Research Article

Mahadevan Govindasamy*, Lloyd Jenner Mangalakaran Joseph Manuel, and Senthilkumar Thamilkolunthu

Influence of shielding gas on machining and wear aspects of AISI 310-AISI 2205 dissimilar stainless steel joints

https://doi.org/10.1515/htmp-2022-0262 received June 14, 2022; accepted November 28, 2022

Abstract: In this article, the effect of shielding gas combinations on gas tungsten arc-welded dissimilar AISI 310 steel and AISI 2205 steel joints was investigated. Two gases such as nitrogen and carbon dioxide were substituted in argon shielding gas and its corresponding improvement in the mechanical, microstructural, machining, and wear aspects of the dissimilar AISI 310-AISI 2205 joints was studied. Weld bead studies, tensile, and weld region microhardness were conducted. X-ray diffraction studies revealed joint intermetallics, and microstructural evaluation was conducted. Machining studies were conducted using drilling experiments. Using local analysis and global analysis, the cutting force variations in the feed direction and cutting direction were studied. Wear tests revealed that the variations in traction force, specific wear rate, coefficient of friction and tribo wear mass loss were studied. A considerable improvement in wear characteristics of AISI 310-AISI 2205 joints was observed by substituting CO₂ and N in shielding gas.

Keywords: shielding gas, carbon dioxide, nitrogen, AISI 310, AISI 2205, machining, wear

1 Introduction

Dissimilar steel joints are being preferred in thermal power plants (radiant tubes, fluidized-bed combustors) [1], automotive (chassis, vehicle body) [2], and aerospace sectors [3]. Many advancements in welding technology have been evident in the recent times [4]. Even then, there is a need to exhibit a better control over welding process and there is scope for improving arc stability during dissimilar welding [5]. Issues, such as carbon migration and un-even weld beads' improper zone formation, occur during the dissimilar welding [6]. Industrial and manufacturing sectors require increased production rate at reduced costs [7]. Studies have been conducted on welding arc voltage variations [8], welding speed [9], welding current [10], electrode diameter [11], polarity [12], cooling time [13], fusion area [14], heat-affected zone (HAZ) area [15], fusion boundary length [16], cooling time [17], and weld bead shape, width, and depth of penetration [18]. In the dissimilar welding, the selection of welding parameters is important.

AISI 310 stainless steels (SSs) are being used in hightemperature environments. AISI 2205 duplex steels consist of austenite and ferrite and are preferred in offshore structures. Both AISI 310 and AISI 2205 steels exhibit excellent mechanical properties and corrosion resistance. AISI 310 austenitic SSs are being used in thermal power plants and nuclear industries for high-temperature applications [19]. During welding of AISI 310 steels, delta ferrite prevents solidification cracking and its dendritic grain structure increases fatigue resistance [20]. AISI 2205 duplex stainless steel (DSS) is being widely used in the nuclear and thermal power sectors as it exhibits high strength, good weldability, and corrosion resistance [21]. Many researchers have attempted to study the characteristics and weldability of AISI 2205 DSS with different welding processes [22,23]. Investigations were done to study the mechanical properties [24], microstructural

^{*} Corresponding author: Mahadevan Govindasamy, Department of Mechanical Engineering, University College of Engineering, Anna University, Tiruchirappalli, 620 024, Tamil Nadu, India, e-mail: gmahadevan80@aubit.edu.in, tel: +91-9942278716

Lloyd Jenner Mangalakaran Joseph Manuel: Department of Mechanical Engineering, University College of Engineering, Anna University, Tiruchirappalli, 620 024, Tamil Nadu, India, e-mail: karanliron@gmail.com, tel: +91-9443532502

Senthilkumar Thamilkolunthu: Department of Mechanical Engineering, University College of Engineering, Anna University, Tiruchirappalli, 620 024, Tamil Nadu, India, e-mail: kmtsenthil@gmail.com, tel: +91-9443267846

aspects [25], and texture studies [26] on AISI 2205 DSS-welded joints. There is a lot of scope for improving the joint characteristics of dissimilar joints. Using the fusion welding techniques, dissimilar joints have certain issues like intermetallic formation, improper Cr fusion, etc. Excessive ferrites and nitride phases are formed in the weld region of dissimilar combinations.

Shielding gas variations and mixes during welding processes affect the weld bead width and depth of penetration [27]. Incorporation of N₂ in shielding gas during gas tungsten arc welding (GTAW) caused shrinkage of arc plasma and improved fusion area [28]. Similarly, carbon dioxide substitution in shielding gas caused narrowing and deepening of welds. Addition of gases such as nitrogen and carbon dioxide affected the residual stresses in welds. It helped to improve the tensile characteristics of the welded joints [29]. As N₂ dissolves in solid solution, the strength of austenite and ferrite increased. The presence of N2 in shielding gas has many advantages. In duplex steel welds, the presence of N2 resulted in the improved austenite content [30]. Toughness of GTAW joints of SSs improved due to the presence of N₂ [31]. In weld pool, N2 increases arc voltage. This improves the concentration of heat. In steel welds, N2 improves overall joint strength [32] and corrosion resistance [33]. Incorporating small quantity of CO2 in shielding gas during welding resulted in increased arc density and arc stability [34]. It enabled the guicker joint fabrication. Pure Ar exhibits greater surface tension and lower thermal conductivity compared to CO₂. Incorporation of CO₂ helps in better weld penetration [35]. Weld pool fluidity improved and ionization energy increased on using CO2. It increased dilution rates at the same arc energy level [36]. An increase in CO₂ substitution improved the contribution of base metal, increased the O2 content, and reduced the contribution of filler material to the welded joints [37].

Machinability aspects of joints should be studied as they are very important in manufacturing. Drilling experiments are used to identify the variations in cutting forces in the welded region. Drilling studies help in evaluating residual stresses in the welds and tool life [38]. Tribological investigations in welded joints help

in predicting the life and durability of the joints in tough environments. From literatures and previous investigations, cutting force studies and tribological investigations on dissimilar steel joints were found to be less. Studies relating to the comparison of dissimilar steel welds using N and CO₂ incorporated shielding gas were not found.

Hence, in this investigation, cutting force analysis (using overall analysis and local analysis approaches) during drilling studies and tribological analysis on gas tungsten arc-welded AISI 310–AISI 2205 steel joints (using N_2 - and CO_2 -incorporated shielding gas) were studied.

2 Materials and methods

The base materials used in this investigation were AISI 310 SS (Stainless Steel) and AISI 2205 DSS (Duplex Stainless Steel). Both were purchased as rolled sheets of 5 mm thickness from M/s. Kheteshwar Metals (India) Goregaon, Mumbai, Maharashtra. In ER2205 filler wire, the ferrite content is lower compared to that of base material. This ensures better weldability [39]. The structure of 2205 steels at fusion temperature is largely comprised of ferrite. ER2205 filler wire retards the rate of cooling. This enables reformation of austenite without intermetallics and improves weld toughness [40]. ER310 filler wire increases sensitization in HAZs, which leads to intergranular corrosion and hot cracking [41]. Hence, 2.6 mm ER 2205 filler wire was used in the experiments. Workpieces were sectioned to 150 mm in length and 100 mm in breadth. They were thoroughly cleaned to remove dirt, oil, and impurities. Single V butt joint configuration was used for all experiments. ASTM E8M 04 (ISO 9692-1:2013) was used for V groove preparation. A V groove angle of 40° and a root gap of 1.2 mm were maintained for all welds. Using clamps, the workpieces were arrested during welding. Using an indigenously developed GTAW welding setup, with double shielding gas input controller, welding experiments were performed. From previous investigations [42-45] and trial experiments, the GTAW welding process parameters were selected

Table 1: Designation of specimens and GTAW process parameters used to weld AISI 310 SS and AISI 2205 DSS

S no	Designation	Shielding gas combination	Welding current (A)	Welding voltage (V)	Welding speed (mm·s ⁻¹)	Gas flow rate (L·min ⁻¹)	Backing gas flow rate (L·min ⁻¹)
1	W-A	100% Ar	90	14	4	8	7
2	W-3C	97% Ar + 3% CO ₂					
3	W-3N	97% Ar + 3% CO ₂					

and are shown in Table 1. With the 3% substitution of N₂ and CO₂ in Ar, experiments were conducted. The designation of AISI 310-AISI 2205 joints is shown in Table 1. The welding setup is shown in Figure 1.

Six sets of joints were fabricated and one set with pure Ar shielding gas for comparison. Tensile studies were conducted using (INSTRON-Make, capacity -60 kN) universal testing machine. Microhardness tests were conducted using the Vickers microhardness testing equipment. Microstructural investigations were conducted using the scanning electron microscopy (SEM) (Make -Carl ZEISS MultiSEM 506). Machining studies were done using the vertical radial drilling equipment. Tribological investigations were conducted using the pin on disc tribo wear equipment (Make – Ducom).

3 Results and discussion

3.1 Chemical composition of base materials

Using spark spectrometer, the elemental composition in weight percentage was evaluated. The chemical composition of the base materials and filler wire is shown in Table 2.

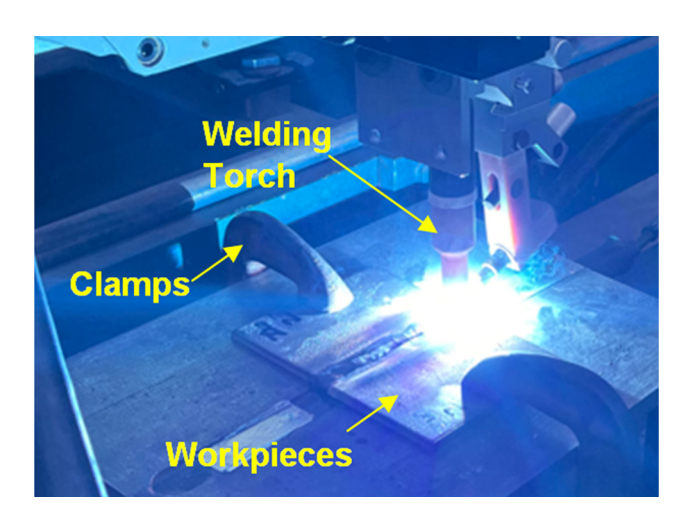


Figure 1: Welding setup used in AISI 310-AISI 2205 welding.

3.2 Weld bead studies

Dissimilar GTAW joints of AISI 310 SS and AISI 2205 DSS were prepared and their weld quality was inspected. On visual inspection, the weld beads were found to be geometrically consistent. It was observed that shielding gas mixes reduced the weld bead width at the face and root sides. Compared to W-A joints, W-3C and W-3N exhibited 6.1 and 7.3% reduction in weld bead width at the face side and 5.8 and 6.9% reduction in weld bead width at the root side, respectively. The dimensions of the three joints are shown in Table 3.

This reduction in weld bead dimension is attributed to the activity of N [46] and uptake of CO₂ [47] in the arc zone. The cross-sections of the three joints are shown in Figure 2.

CO₂ uptake in the weld region induces constriction of arc and deeper weld penetration [48]. In the W-3C specimen, incorporation of CO₂ caused reduction in root and face of the dissimilar joint, due to the peculiar behavior of CO₂ in shielding gas [49]. N is not an active gas and it does not increase heat in weld pool. In the interface region between fusion zone and base material, the presence of N lesser than 4% in shielding gas causes reduction in turbulence [50]. In the W-3N specimen, the presence of N in shielding gas caused the weld bead width to reduce.

3.3 Tensile studies

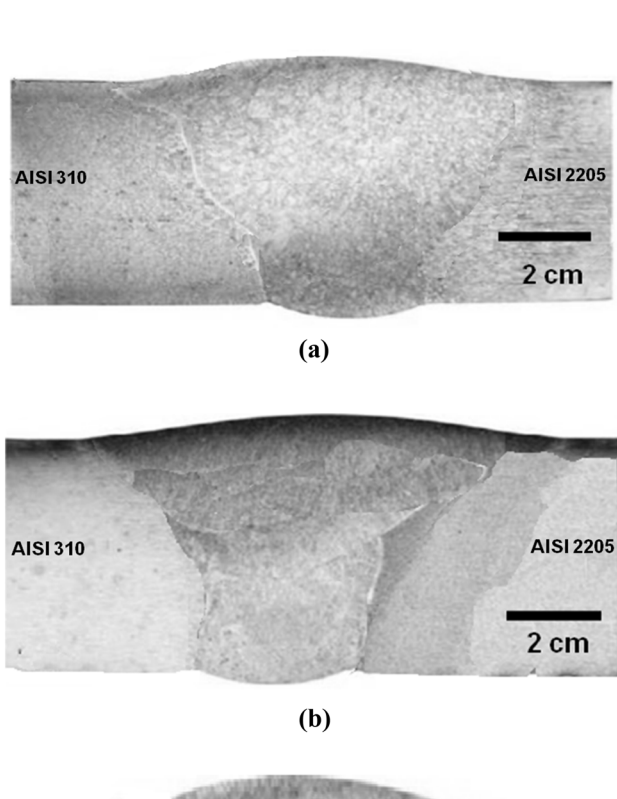
The as-received base materials and welded samples were subjected to tensile tests as per ASTM E-08 standards. Using an electro-pneumatically controlled Universal Testing Machine (Make-Instron, Capacity - 60 kN), the tensile experiments were conducted. On evaluating the tensile strength of base materials, yield strength (YS) and ultimate tensile strength (UTS) of AISI 2205 DSS were 2.28 and 1.14 times greater than that of AISI 310 SS material. For evaluating the joint strength, the lower strength alloy (AISI 310 SS) was chosen for comparison. The YS of W-A, W-3C, and W-3C was found to be 81.2,

Table 2: Chemical composition of base materials and filler wire (wt%)

Material	Cr	Ni	Мо	С	Mn	Si	Р	S	Fe
Base metal AISI 310 SS	24.3	19.8	_	0.19	1.1	1.3	0.009	0.01	Bal
Base metal AISI 2205 DSS	22.4	4.82	3.16	0.02	1.6	0.71	0.018	0.02	Bal
Filler wire ER 2205	22.3	8.29	2.69	0.01	1.3	0.34	0.014	0.34	Bal

Table 3: Weld bead dimensions

S no	Joint	Weld bead width welding current (A)	nt (A)	Quality inspection
		Face side (mm)	Root side (mm)	
1	W-A	6.36	5.21	Longitudinal microcracks with inter running undercuts were visible
2	W-3C	5.97	4.90	Porosities due to lack of fusion were observed. Surface gas pores were formed
				due to the trapping of gases in small quantities within the molten weld puddle [51] during solidification
3	W-3N	5.89	4.85	Minor external discontinuities due to tubular gas cavities were observed. They
				were due to modifications in shielding gas composition [52]. Longitudinal and
				microcracks were observed



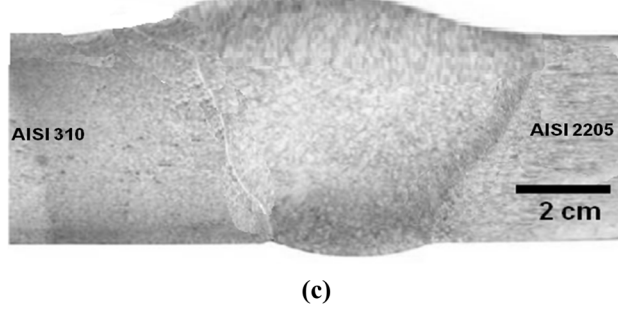


Figure 2: Cross-section of (a) W-A, (b) W-3C, and (c) W-3N.

84.9, and 86.8%, respectively, of the YS of the base material AISI 310 BM. The UTS of W-A, W-3C, and W-3C was found to be 83.4, 88.7, and 89.6%, respectively, of that of the base material AISI 310 BM. Reduction in the percentage of elongation was observed for all the joints.

Out of the three, W-3N joints exhibited better percentage of elongation compared to W-A and W-3C. The results of tensile test results are shown in Table 4. The stress–strain graphs of tensile tests are shown in Figure 3. During tensile tests, fracture of the three W-A, W-3C, and W-3N specimens occurred in the HAZ. All three fractures occurred on the HAZ of AISI 310 sides. SEM images of the fractured surfaces are shown in Figure 4.

Figure 4a shows SEM fractograph of W-A specimen. Fracture morphology indicates the presence of dendrites. The presence of dendrites caused the fracture to change from ductile to brittle [53]. Figure 4b shows the

Table 4: Tensile test results

Material	YS (MPa)	UTS (MPa)	Percentage of elongation
AISI 310 SS	213	439	21.3
AISI	486	619	23.4
2205 DSS			
W-A	173	366	16.8
W-3C	181	389	17.2
W-3N	185	393	18.1

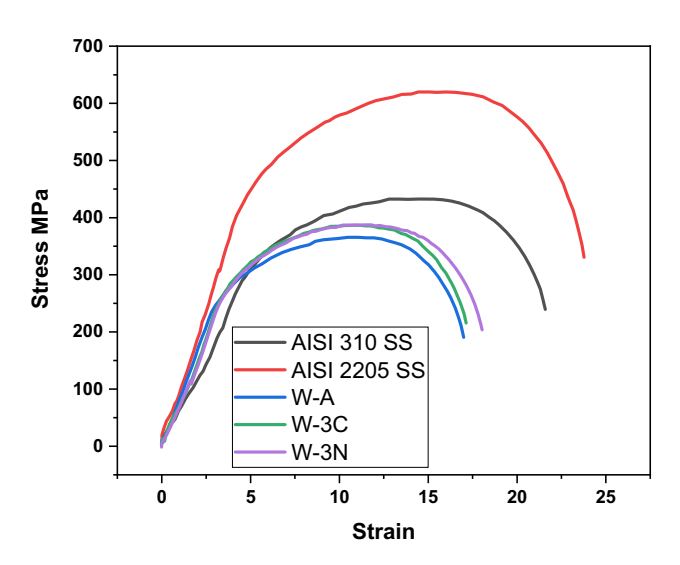
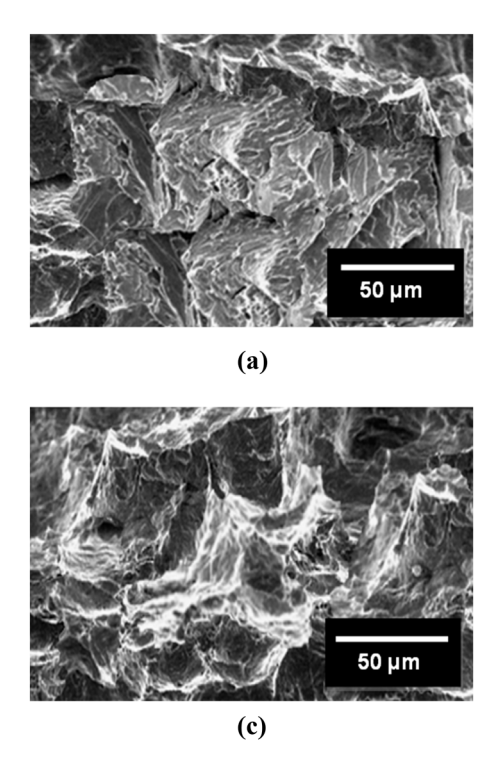


Figure 3: Stress-strain graphs of tensile-tested specimens.



fracture morphology of W-3C specimen. Mixed fracture morphology was observed. Cleavage-type fractures were observed in certain regions. The fracture was more ductile due to the presence of annealed austenitic grains [54]. These attributed to the better tensile properties of W-3C samples, compared with W-A samples. Figure 4c shows the fracture morphology of W-3N specimens. Fracture was ductile as wider dimples were observed. The presence of wide dimples indicates better strength [55].

3.4 Microhardness studies

Microhardness tests were conducted as per ASTM E 384 standards. Using Vickers hardness testing equipment, microhardness testing was conducted. As per ASTM E 384 standards, a load of 5 kgf was placed on the indenter for a dwell time of 15 s. The indentation in the specimen was evaluated to identify the microhardness values. Microhardness variation at a distance of every 200 μm from weld region, for AISI 310 SS–AISI 2205 DSS joints made by using shielding gas mixes, was measured. Variations in microhardness across the welds for the three joints, with their microstructures, are shown in Figure 5. The width of the weld zone, HAZ on AISI 2205 SS side, and AISI 310 SS side were identified and they are shown in Table 5.

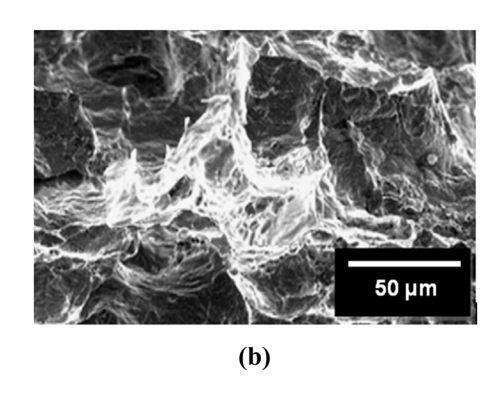
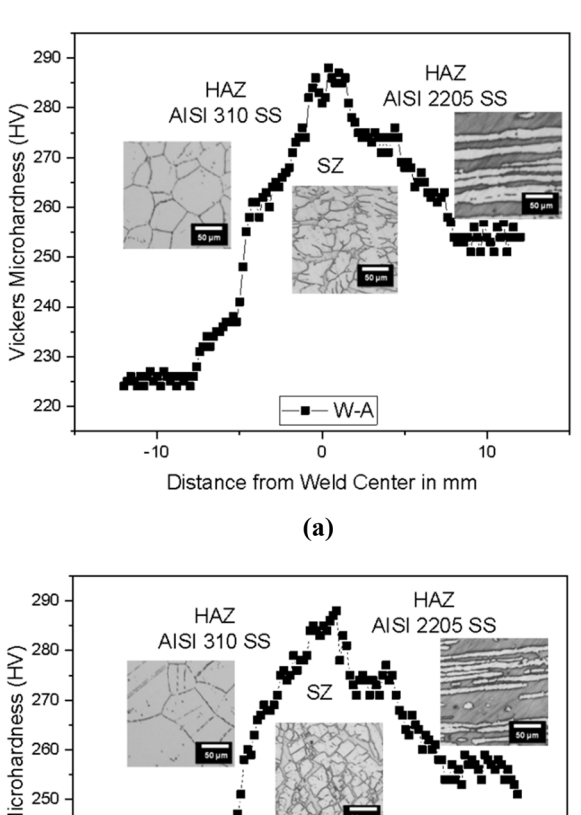
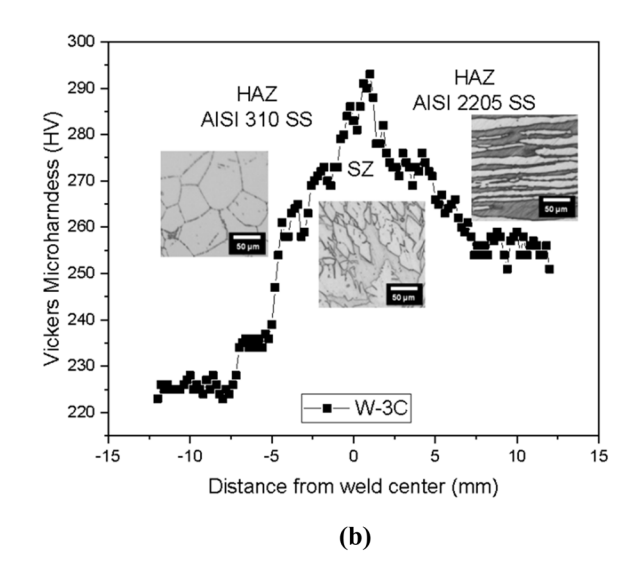


Figure 4: SEM images of fractured (a) SEM fractograph of W-A, (b) SEM fractograph of W-3C, and (c) SEM fractograph of W-3N.





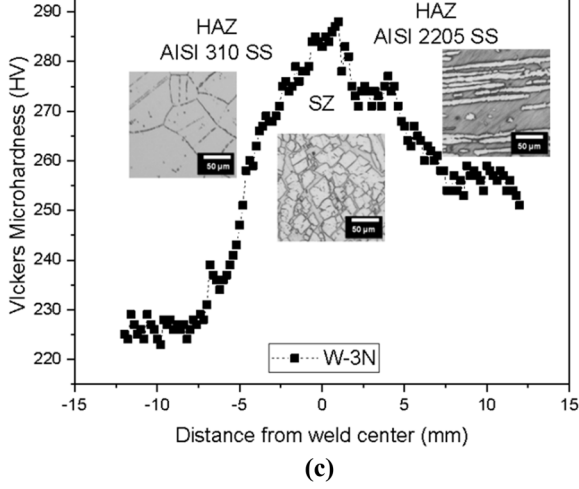


Figure 5: Microhardness variations across the weld. (a) Microhardness distribution across W-A, (b) microhardness distribution across W-3C, and (c) microhardness distribution across W-3N.

Table 5: Width of HAZ for the joints (in cm)

HAZ	AISI 2205 SS side	AISI 310 SS side
W-S	0.439	0.387
W-N	0.412	0.374
W-C	0.398	0.359

Upon investigating the microhardness variations across the dissimilar joints, in all three joints, the microhardness in the fusion zone was higher than the microhardness of the parent materials. Microhardness at the HAZ of both AISI 2205 DSS side and AISI 310 SS side reduced as a negative slope from the weld zone to base material (BM).

The presence of N in the fusion zone induces grain refinement. Hence, a small reduction in microhardness

was observed in the fusion zone for joints fabricated using shielding gas mix of N compared to welds made using shielding gas mix of CO₂. From the interface region, the microhardness toward AISI 2205 DSS side was consistently higher than the microhardness values toward AISI 310 SS side. Higher microhardness toward AISI 2205 DSS side was attributed to the effect of higher solid solution strengthening along the diffusion region [56]. For W-A, W-3C, and W-3N joints, the average microhardness in the interface region toward AISI 310 SS side was recorded as 258 HV, 263 HV, and 261 HV, respectively, and the average microhardness along AISI 2205 DSS was recorded as 283 HV, 276 HV, and 271 HV, respectively. Microhardness variations in HAZ were found to drastically reduce from the end of fusion zone and the beginning of parent material region.

3.5 X-ray diffraction (X-RD) studies

X-RD studies were conducted on the base materials and welded joints to identify the intermetallic compounds and oxides formed during the GTAW process. X-RD spectrum for the base materials and the joints were recorded and compared with JCPDS data for identifying the elements and compounds present in it. X-RD graphs (Figure 6) of AISI 310 SS consisted of γ-Fe, Cr, and Ni, AISI 2205 DSS exhibited the presence of σ -Fe and δ -Fe, W-A joint consisted of Fe₂O₃, FeCr₂O₄, σ -Fe, γ -Fe, δ -Fe, Cr, and Ni, W-3C joint consisted of Fe₂O₃, FeCr₂O₄, σ -Fe, γ -Fe, δ -Fe, Cr₃C₇, and Cr₂C₃, and W-3N exhibited the presence of Cr₂C₃, Fe₂O₃, FeCr₂O₄, σ -Fe, γ -Fe, δ -Fe, Ni, Cr, and Cr₃C₇. The as-received AISI 310 SS material consisted of σ platelets. The morphology of AISI 310 base material was composed of residual δ ferrite

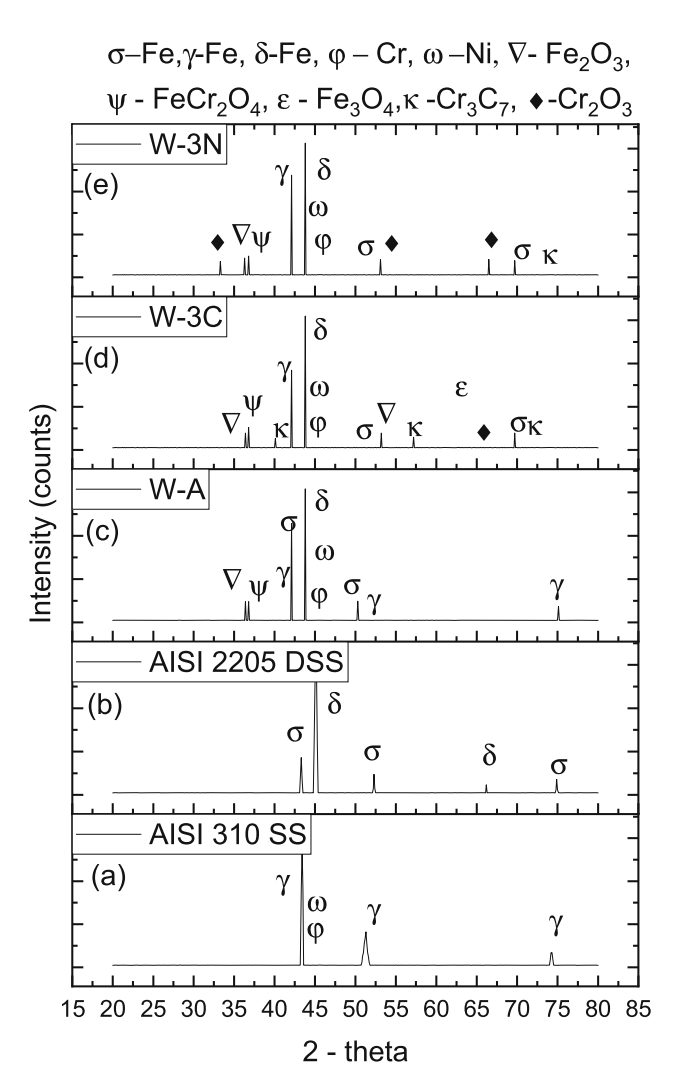


Figure 6: X-RD analysis graphs of (a) AISI 310 SS, (b) AISI 2205 DSS, (c) W-A, (d) W-3C, and (e) W-3N joints.

[57]. Fe₂O₃ formation occurred in welded joints during resolidification, where high-temperature Fe reacted with atmospoheric O₂. When the reaction temperature was beyond 2,000 K, interdiffusion of O₂ through the metal surface caused post-perovskite type Fe₂O₃, to be formed [58].

In austenitic SSs such as AISI 2205, at elevated temperatures, variation in nucleation caused precipitation of σ -Fe. Diffusion of chromium and σ forming elements causes grain growth. Distorted grains indicated the presence of iron oxide. During welding, high temperature causes segregation of Cr and Mo in AISI 2205 [59]. This heat transforms entire structure to ferrite, which reform to austenite grains on cooling down. At the molten stage, at certain cases, the improper diffusion of chromium occurs. This diffusion through ferrite structure induces partially transformed ferrite-austenite structures to be formed. The ratio of ferrite to austenite increases on increasing the welding temperature [60]. On cooling down, resolidification causes reduction in austenitic content. The presence of austenitic content in resolidified region was found to be lower than molten and partially annealed regions [61]. Fe-Cr oxide forms in the outer layer of oxide films. Cr-based oxide forms due to the diffusion of O_2 through the welding pool. The diffusion rate of Cr and Cr ions is relatively slower than other elements. This results in the growth of Cr-based oxides in inner layer [62]. At high temperatures, dissolution of Fe₃O₄ causes the formation of Fe²⁺ ions [63]. By the dissolution reaction process, Fe2+ ions react with Cr2O3 to form FeCr₂O₄ oxide layer [64].

Reduction reaction in the outer oxide film containing Fe_2O_3 with Fe precipitates causes the formation of Fe_3O_4 . Formation of Fe_3O_4 was attributed to the dissolution reaction precipitation [65]. High-temperature interaction between dissolved Ni^{2+} and Fe^{3+} reacts to form $NiFe_2O_4$ precipitates [66].

3.6 Microstructural studies

Surfaces of the weld regions (dissimilar AISI 310 SS and AISI 2205 DSS welds) and the base materials were prepared using conventional metallurgical procedures, for conducting microstructural investigations. Using the SiC emery paper, the surfaces were polished and then by using diamond grit paste they were polished in disc polisher. The surface was etched as per ASTM E-407-07 standards [67]. Etching solution was prepared by diluting 10 mL of oxalic acid in 100 mL of distilled water. The etching voltage was fixed at 6 V. Etching was done on

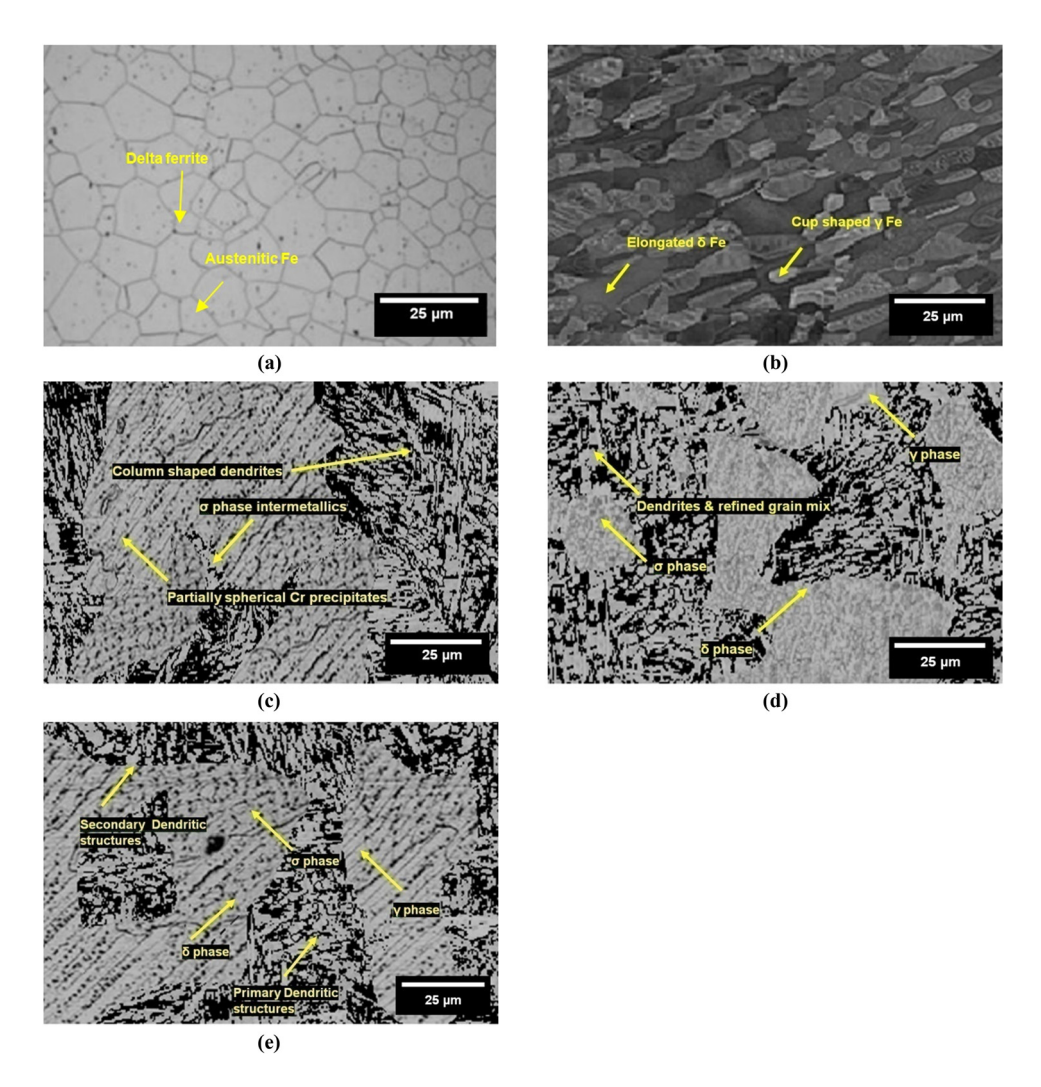


Figure 7: SEM images of (a) as-received AISI 310 SS, (b) as-received AISI 2205 DSS, and weld region of (c) W-A, (d) W-3C, and (e) W-3N.

the specimens for 1 min. SEM images of as-received base materials and welded joints are shown in Figure 7. SEM image of as-received AISI 310 SS (Figure 7a) indicates equiaxed and fine-grained microstructure. This is attributed to the water quenching effect of AISI 310 SS sheets after hot rolling process [68]. In austenite matrix, delta ferrite stringers were observed. Elongation of delta ferrite structures was found to be parallel to that of rolling direction. SEM image of as-received AISI 2205 DSS (Figure 7b) shows restrained austenite as coarse-grained structure. δ Fe was observed as elongated lines in wedge-shaped microstructure and y Fe exhibited cup-shaped structure [69]. SEM image of the weld region of W-A specimen (Figure 7c) indicates porosity and slag-free microstructure. Dendrite-shaped structures around rough cylindrical grains was observed. Isolation of cylindrical grains in dendrite clusters results in grain growth [70,71]. Σ phase intermetallics with the high Cr content was formed due

to ferrite-austenite restructuring [72]. Cr-based elliptical and partially spherical precipitates were found around the dendritic austenite phase. SEM image of the weld region of W-3C specimen (Figure 7d) indicates a mixture of dendritic and finely refined regions. Morphology of W-3C was different from W-A weld zone. W-A exhibited refined microstructure with infrequent dendrite clusters. Intermediate carbide phases with y, δ , and σ phases were found. Coarse cubic structures of chromium carbides were observed [73]. Segregation of σ phase was more than segregation of y phase and δ phase. This variation was attributed to the activity of CO₂ during solidification in weld zone [74]. SEM image of the welded region of W-3N specimen (Figure 7e) indicates hard and distinct σ phases with intermediate phases. Continuously distributed dendrite structures were found in the central part. Ultra-fine structure with primary and secondary dendrite phases was observed due to the interruption imparted by nitrogen [75]. Reformed austenitic structure was observed due to the depletion of N through the weld zone [76].

3.7 Machining studies

DE GRUYTER

The welded joints and the base materials were subjected to drilling experiments and the variations in their cutting forces were recorded. Cutting force variations are shown in Figure 8. The cutting force variations with time for drilling experiments are shown in Figure 8a – 600 rpm spindle speed and feed rate of 5 mm·min⁻¹, Figure 8b – 600 rpm spindle speed and feed rate of 10 mm·min⁻¹, Figure 8c – 1,200 rpm spindle speed and feed rate of 5 mm·min⁻¹, and Figure 8d – 1,200 rpm spindle speed and feed rate of 10 mm·min⁻¹, respectively.

In all the drilling experiments, a rapid increase in cutting forces was observed, during initial drilling time, till the drill bit completely protruded into the work piece. After a few seconds, the cutting forces stabilized and the variations were minimal. On comparing the two base materials, at low and high spindle speeds and feed rates, the cutting forces developed during AISI 2205 DSS drilling were always higher than the cutting forces developed during drilling AISI 310 SS. Higher drilling forces generated in AISI 2205 DSS were due to higher hardness of AISI 2205 DSS than AISI 310 SS. Throughout the experiments, base materials, and welded joints, fluctuations in cutting forces were lesser upon increasing the feed rate. At low spindle speed of 600 rpm, an increase in feed rate caused a significant increase in cutting force. At the stabilized phase, cutting forces in AISI 2205 DSS varied between 300 and 350 N at 600 rpm spindle speed and 5 mm \cdot min⁻¹

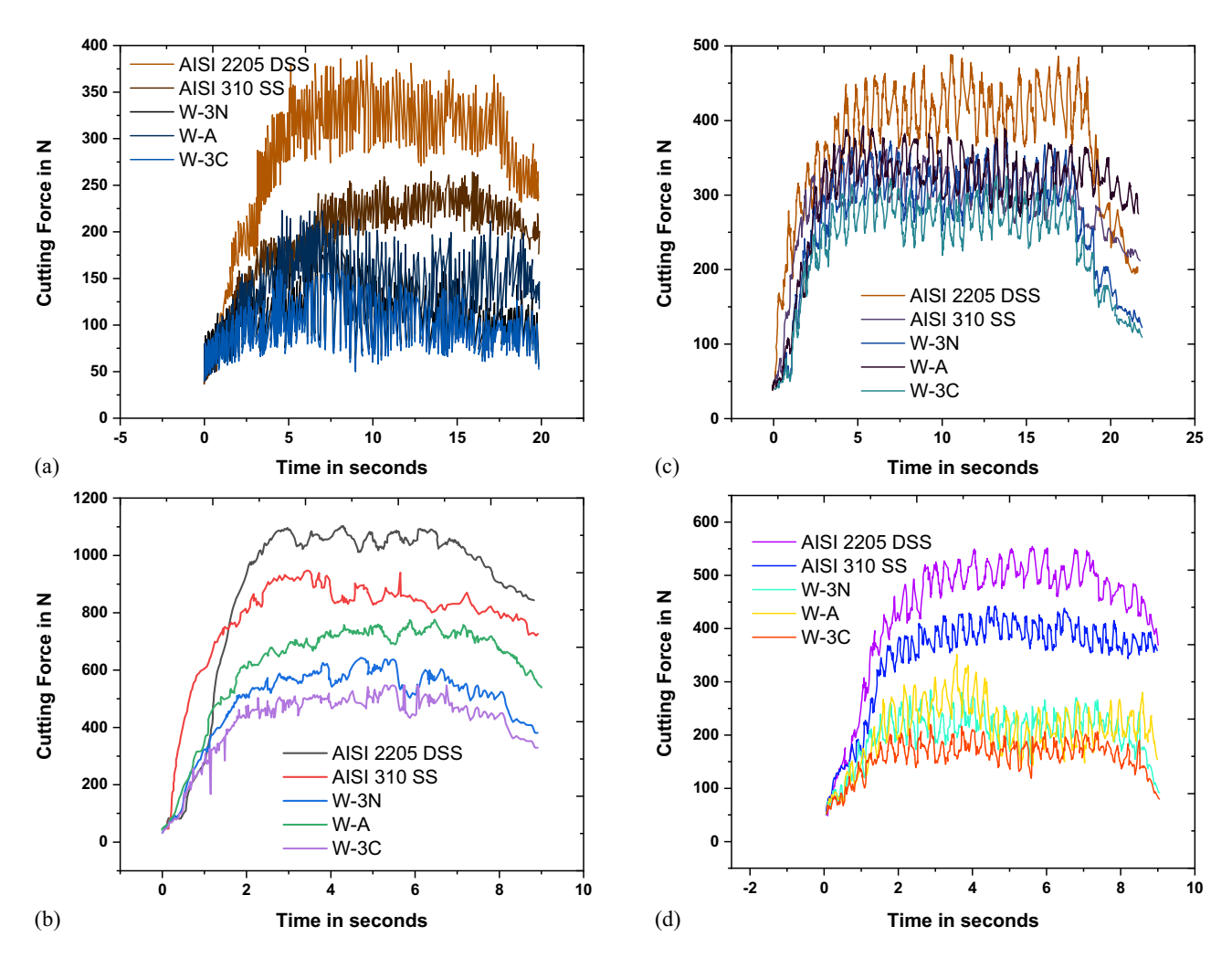


Figure 8: Cutting force profiles at drilling parameters (a) 600 rpm spindle speed and feed rate of 5 mm·min⁻¹, (b) 600 rpm spindle speed and feed rate of 10 mm·min⁻¹, (c) 1,200 rpm spindle speed and feed rate of 10 mm·min⁻¹.

feed rate. The variations were between 950 and 1,050 N on increasing the feed rate to 10 mm·min⁻¹. Such shift in cutting force variations was observed for AISI 310 SS and the welded joints. On comparing the welded joint cutting forces, the cutting force variations in the W-A joint weld region were always greater than the cutting force variations in W-N and W-C joints. The effect of annealing was found to be greater in the joints which we are fabricated using carbon dioxide-substituted shielding gas. Thus, for both low level and high level drilling process parameters, W-3C joints exhibited relatively lower cutting forces than W-3N joints.

Characterization of drilling was focused on the drilling parameters and conditions in which the experiments were performed. With two stages, the drilling forces are characterized. The first stage is until penetration of the drill tip. The second stage is the entire hole drilling process after the drill tip has penetrated into the work piece [77]. With these two stages, the drilling characterization was conducted with two approaches. The first approach is the overall analysis. The second approach is the localized analysis [78].

In overall analysis approach, specific cutting energy (SCE) due to cutting effect $SCE_{c,f}$ and SCE due to margin effect $SCE_{c,c}$ have been analyzed. In the localized analysis approach, the variations in forces along cutting edges during tool tip penetration have been analyzed [79].

3.7.1 Overall analysis approach

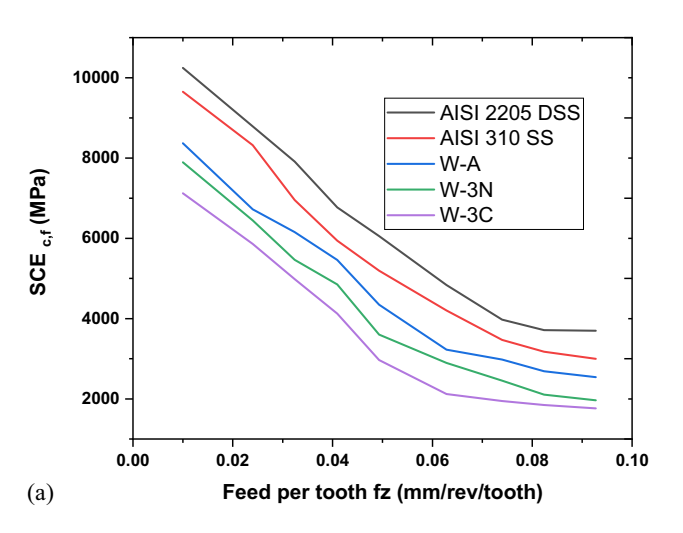
In manufacturing industries, determination of the optimized drilling conditions for minimizing the cutting energy is important [80]. This helps in minimizing the overall energy used and improves tool life [81]. This tool material pair methodology is used for identifying the efficiency of the drills. During the drilling process, the forces developed due to plunge of the rotating tool into the workpiece is divided into two forces. The first one is the feed force (FF_f) and it is measured along the axial drilling direction. The second force is the tangential force (TF_c), which acts on the cutting edge. This tangential force is responsible for creating a cutting torque (T_c). CF_z is the cutting force generated during drilling, f is the feed, and D is the tool diameter. During steady-state conditions, the mean value of the cutting forces was used to calculate SCE_{c,f} and SCE_{c,c}, according to the following equations [80]:

$$SCE_{c,f} = \frac{2 \times CF_z}{D \times f},$$
 (1)

$$SCE_{c,c} = \frac{H \times CF_z}{D \times f}.$$
 (2)

Value of *H* was taken as 8,000, according to NF E66-520-8, 2000, standard.

Figure 9 shows the results for variations in specific cutting energies while varying the feed per tooth (mm·rev $^{-1}$) from 0.01 to 0.10 mm·rev $^{-1}$. The fluctuations in SCE $_{c,f}$ are shown in Figure 9a and the fluctuations in SCE $_{c,c}$ are shown in Figure 9b. For ease of comparison, the graph has been plotted in feed rate per tooth. A drastic decrease in SCE $_{c,f}$ and SCE $_{c,c}$ was observed upon increasing the feed rate [81]. SCE $_{c,f}$ and SCE $_{c,c}$ of AISI 2205 DSS were higher than that of AISI 310 SS base material. Regarding the welded joints, W-A recorded the highest and then, W-3N and W-3C recorded the lowest. SCE $_{c,c}$ variations were lower compared to the variations in SCE $_{c,f}$ for the different joints. This attributes to higher sensitivity of penetration



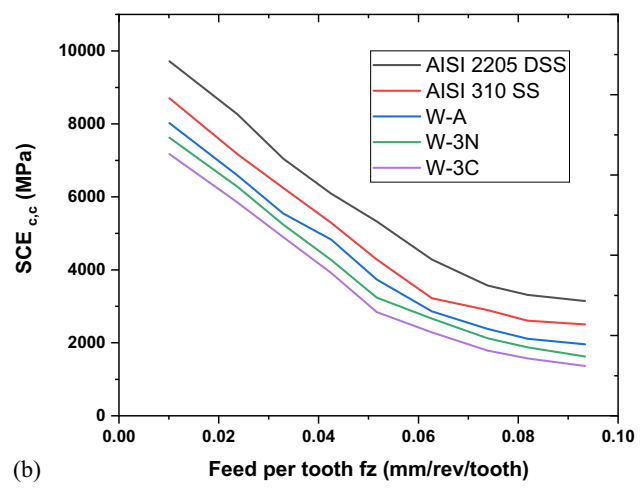


Figure 9: Specific cutting force in (a) feed direction and (b) cutting direction.

force to cutting geometry than torque [82]. The specific energy in W-3N during chip formation was higher than that of W-3C. Due to higher hardness, the mechanical load on W-3N was higher than that on W-3C. Chisel edge of the drill consists of negative cutting geometry (Rake angle $\gamma_n = -60^{\circ}$). Such high negative geometry induces more pressure on the cutting edges and increases ploughing rather than chip formation [83].

3.7.2 Local analysis approach

Local analysis approach is to evaluate the forces generated in the chisel edge and cutting edge during penetration of the drill bit into the work piece. This analysis is conducted based on the instantaneous force and torque generated during drilling. Contribution of the cutting edges on the overall cutting forces has been identified by using edge discretization methodology [84]. Figure 10 indicates the various forces developed during tool tip penetration.

Progressive increase in cutting edge occurs from axis to drill corner during drilling operation. Overall forces evolve as a function of tool radius R, linked to tool position z. Therefore, the local force developed in the feed direction LF_{fi} and cutting direction LF_{ci} on the nth cutting edge is calculated according to the following equation [85]:

$$LF_{fn} = \frac{Ff_{n+1} - Ff_n}{D \times f},$$
(3)

$$LF_{cn} = \frac{Mc_{n+1} - Mc_n}{R_n} \times \frac{1}{Z \times Q_e}.$$
 (4)

In the above equations

$$R_n = z_n \times \tan[\alpha_{\rm rn}],\tag{5}$$

$$Q_{\rm e} = \frac{\mathrm{d}z_n}{\cos(\alpha_{\rm rn})}. (6)$$

Under similar cutting conditions of axial spindle velocity of 5 mm·min⁻¹ and $f_z = 0.008$ mm·rev⁻¹ per tooth, the cutting forces were traced from the axis of the drill to the periphery. Figure 11 shows the variations in local forces. Figure 11a shows the forces developed in the feed direction (LF_{fi}) and Figure 11b shows the local forces developed in cutting direction (LF_{ci}).

From Figure 10, local force generated in feed direction and cutting direction was found to be highest at the center of the twist drill. The forces gradually reduced upon moving toward periphery. On the whole, LF_f was significantly higher than LF_c. Due to high hardness, LF_f and LF_c variations in AISI 2205 DSS were maximum, compared to AISI 310. After AISI 310 SS, W-A joints exhibited higher LF_f and LF_c than W-3N and W-3C. As weld region grain refinement was more in W-3C joints than in W-3N joints, LF_f and LF_c of W-3C were lower than that of W-3N. As the rake angle of the twist drill was highly negative, the cutting forces generated in the center edge was very low.

3.7.3 Effect of drilling conditions on local cutting forces

Local specific cutting forces such as LF_f and LF_c were evaluated from global cutting forces such as SCE_{c f} and SCE_{c.c}. Local specific cutting forces in the feed direction

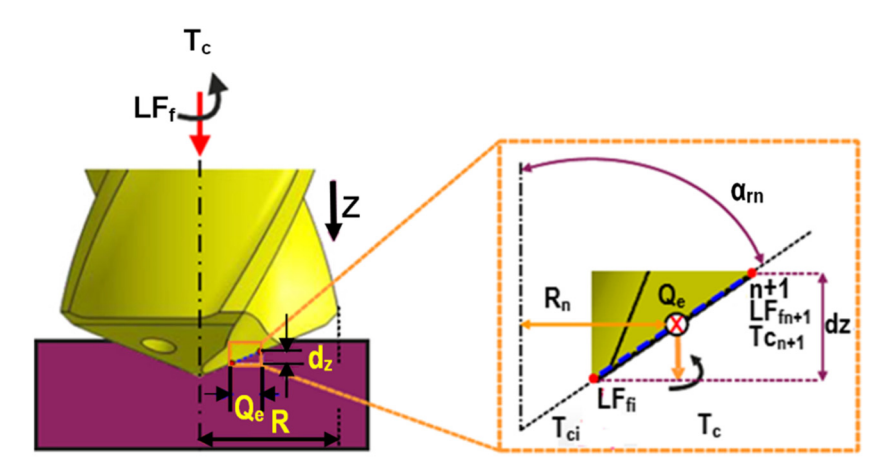


Figure 10: Various forces developed during drill tip penetration.

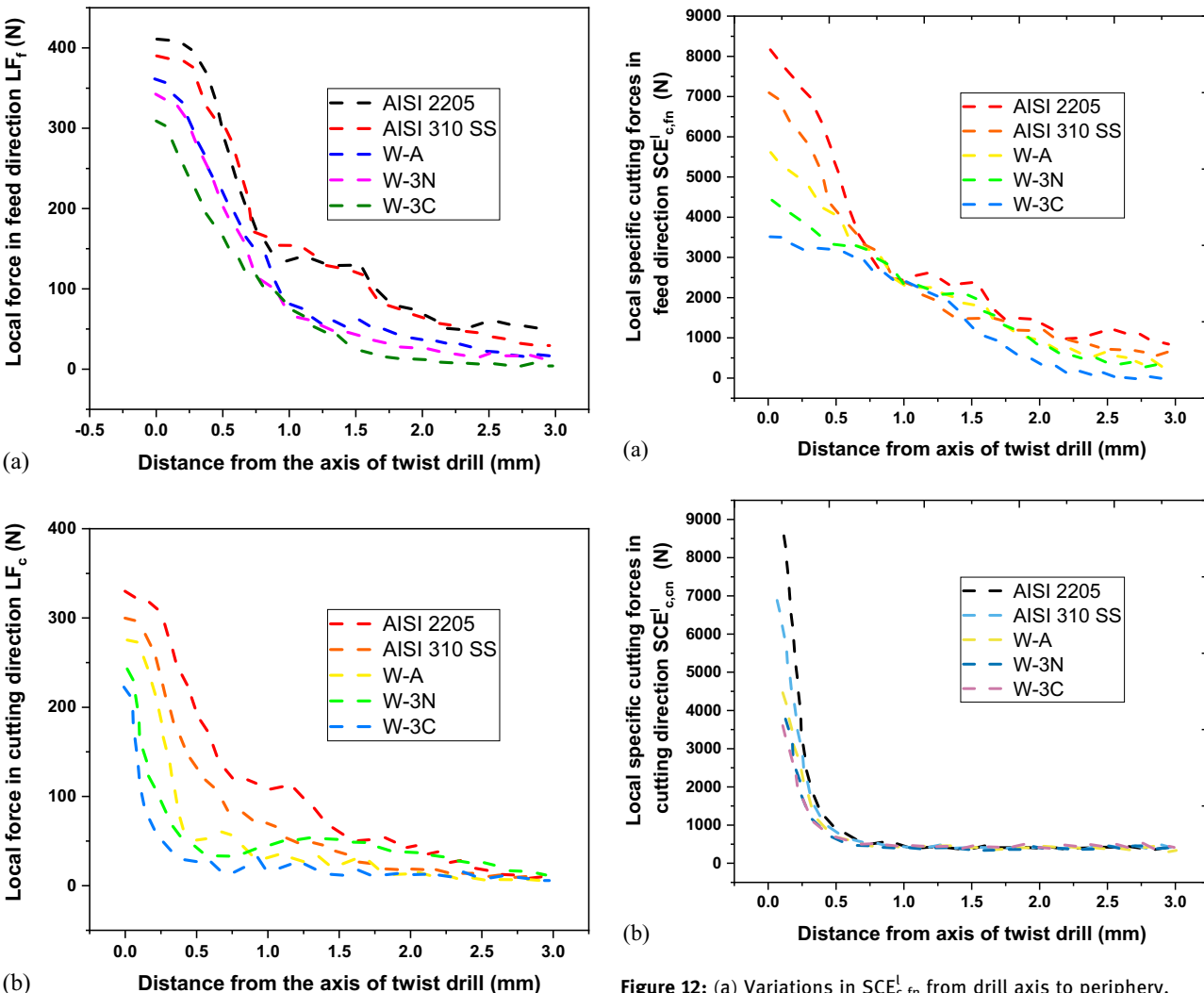


Figure 11: (a) Variations in feed force LF_f from drill axis to periphery.

(b) Variations in cutting force LF_c from drill axis to periphery.

 $SCE_{c,f}^{l}$ and along cutting direction $SCE_{c,c}^{l}$ are calculated according to the following equation [86]:

$$SCE_{c,fn}^{l} = \frac{LF_{fn}^{l}}{f_{z} \times \sin \alpha_{rn}},$$
 (7)

$$SCE_{c,cn}^{l} = \frac{LF_{cn}^{l}}{f_z \times \sin \alpha_{m}}.$$
 (8)

Figure 12 shows variations in local specific cutting forces from twist drill axis to periphery. Figure 12a shows $SCE^l_{c,fn}$ variations from drill axis to periphery and Figure 12b shows $SCE^l_{c,cn}$ variations from drill axis to periphery. A considerable decrease in forces at the chisel edge zone was observed for all three joints.

 $SCE_{c,fn}^l$ and $SCE_{c,fc}^l$ at axis (chisel edge) were found to be high and decreased toward periphery. At chisel edge, $SCE_{c,fn}^l$ of welded joints was lower than that of the base

Figure 12: (a) Variations in $SCE_{c,fn}^l$ from drill axis to periphery. (b) Variations in $SCE_{c,fc}^l$ from drill axis to periphery.

materials. $SCE_{c,fn}^l$ of W-A, W-3N, and W-3C was found to be 28, 36, and 42% lower than $SCE_{c,fn}^l$ value of AISI 2205 DSS, respectively (Figure 12a). Similarly, $SCE_{c,cn}^l$ of W-A, W-3N, and W-3C was found to be 33, 39, and 46% lower than $SCE_{c,cn}^l$ value of AISI 310 SS, respectively (Figure 12b). As the rake angle of the twist drill was highly negative, the ploughing of chisel edge on W-3N was greater than W-3C samples.

3.8 Wear tests

High Speed Steel-Cobalt (HSS-Co) twist drill of 6-mm diameter with three teeth was used for drilling. Cutting force dynamometer was fixed in the bed of a vertical milling computer numerically controlled machine and on the dynamometer, the drilling work pieces were fixed. At two different spindle speed (600 and 1,200 rpm) and two different feed rates (5 and 10 mm·min⁻¹), drilling

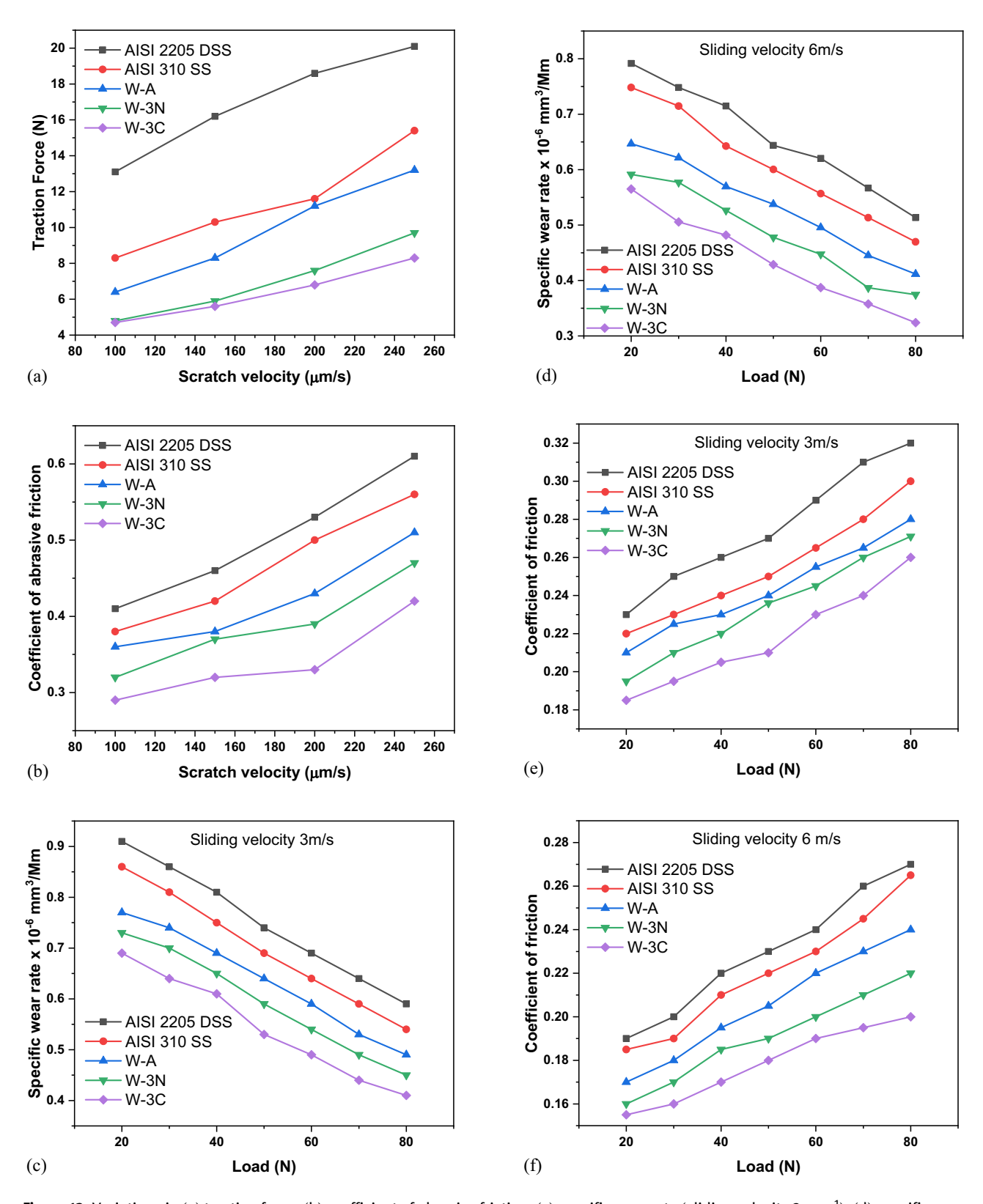


Figure 13: Variations in (a) traction force, (b) coefficient of abrasive friction, (c) specific wear rate (sliding velocity 3 m·s⁻¹), (d) specific wear rate (sliding velocity 6 m·s⁻¹), (e) coefficient of friction (sliding velocity 3 m·s⁻¹), (f) coefficient of friction (sliding velocity 6 m·s⁻¹), (g) wear mass loss (sliding velocity $3 \text{ m} \cdot \text{s}^{-1}$), and (h) wear mass loss (sliding velocity $6 \text{ m} \cdot \text{s}^{-1}$).

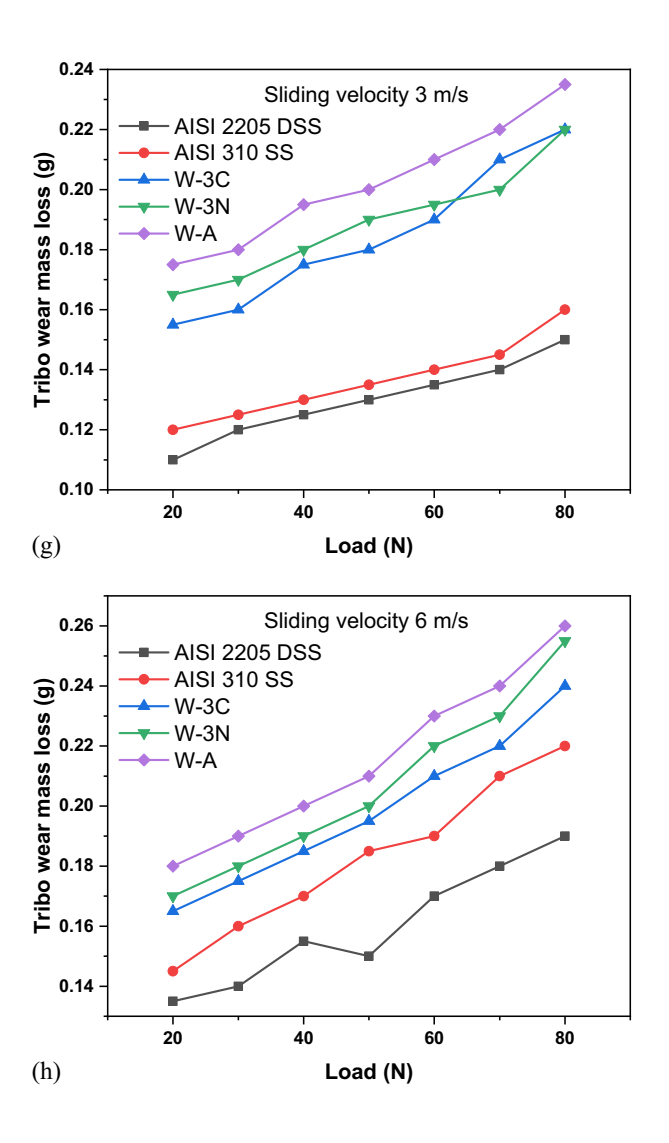


Figure 13: (Continued)

experiments were conducted and the variations in cutting forces were identified. As per ASTM C-1624 standards, microscratch tests were conducted on the welds to identify the traction force and coefficient of abrasive friction [87]. With 20 N load, scratches were done on the welds for 15 mm length. At four different scratching velocities such as 100, 150, 200 and 250 µm·s⁻¹, the experiments were conducted and the offset was set at 2 mm. Before conducting microscratch tests, the specimens were poised using emery sheets. As per ASTM G99-17 standards, the pins were prepared from the weld region. HSS disc of 100 mm diameter was used as the rotating disc, with track diameter of 60 mm. Wear experiments were conducted in dry conditions, without lubrication. Two sliding speeds were used (3 and 6 m·s⁻¹) and load on the pins were varied from 20 to 80 N. Wear tests were conducted for a duration of 5 min and the variations in wear mass loss, coefficient of friction and specific wear rate were identified.

The variations in traction force during microscratch experiments for the base materials and welded joints are shown in Figure 13a and the variations in coefficient of abrasive friction or the base materials and the welded joints are shown in Figure 13b. The variations in specific wear rate, coefficient of friction, and wear mass loss at sliding velocity of 3 m·s⁻¹ are shown in Figure 13c, e, and g, respectively. Similarly, the variations in specific wear rate, coefficient of friction, and wear mass loss at sliding velocity of 6 m·s⁻¹ are shown in Figure 13d, f, and h, respectively.

Regarding traction force (Figure 13a) and coefficient of abrasive friction (Figure 13b), for the base materials and the welded joints, a consistent increase was observed upon increasing the scratching velocity from 100 to 250 $\mu m \cdot s^{-1}$. AISI 2205 DSS exhibited the highest, followed by AISI 310 SS base material. On comparing the welded joints, W-A exhibited higher traction force and coefficient of abrasive friction, followed by W-3N and

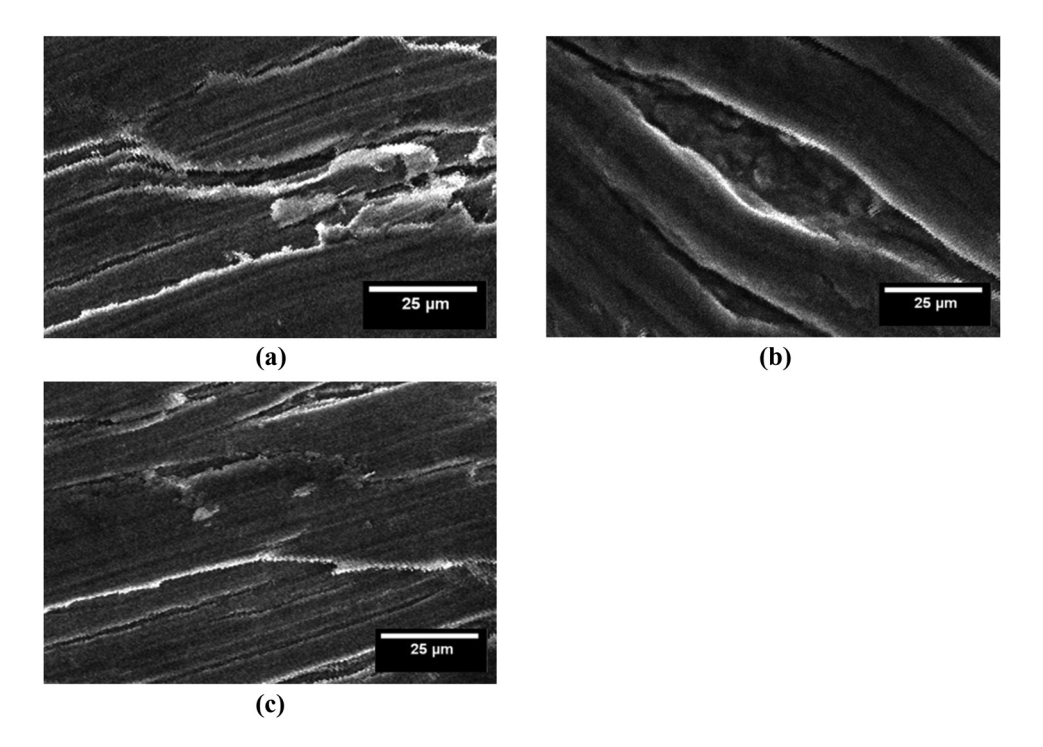


Figure 14: SEM images of wear-tested specimens of (a) SEM image of wear-tested W-A, (b) SEM image of wear-tested W-3C, and (c) SEM image of wear-tested W-3N.

W-3C. Traction force was calculated under dry conditions, without lubrication. The deformations in the surface owing to the microcontact of the traction pin at different velocities attribute to the increase in traction force, upon increasing the scratching velocity [88].

Specific wear rate (Figure 13c) was found to decrease consistently, upon increasing the loading from 20 to 80 N. The base material-specific wear rate of AISI 2205 DSS was highest, followed by AISI 310 SS. Then, it was followed by the specific wear rate variations in W-A. W-3N, and W-3C joints. Similar pattern was observed upon increasing the sliding velocity from 3 to 6 m·s⁻¹ (Figure 13d). The entire graph of specific wear rate was found to shift downwards, upon increasing the sliding velocity from 3 to 6 m·s⁻¹. An increase in sliding speed caused a quantified reduction in specific wear rates, for the base materials as well as the welded joints. Coefficient of friction (Figure 13e and f) increased upon increasing the loads, for both the base materials and the welded joints. For all loads, AISI 2205 DSS exhibited highest coefficient of friction, followed by AISI 310 SS, W-A, W-3N, and W-3C. It was found that the presence of N and CO₂ in the weld region of W-3N and W-3C caused grain refinement. This caused a reduction in coefficient of friction, compared to the joints fabricated without shielding gas mixes (W-A). The coefficient of friction for base materials and welded joints reduced upon increasing the sliding velocity, due to reduction in plastic deformation at higher sliding speeds [89].

Tribo wear mass loss (Figure 13g and h) was minimum for AISI 2205 DSS, on all loading conditions due to its superior hardness and strength. Tribo wear mass loss for AISI 310 SS was slightly higher than AISI 2205 DSS. On comparing welded joints, W-3C exhibited greater resistance to wear than W-3N. W-A exhibited least wear resistance, compared to the other two. Wear-tested specimens were subjected to microstructural evaluation using SEM imaging. SEM image of wear-tested W-A, W-3C and W-3N is shown in Figure 14a-c. SEM image of wear-tested W-A specimen (Figure 14a) indicated microlips, cuts, and prows [90]. SEM image of wear tested W-3C specimen (Figure 14b) revealed microploughs and flake-shaped pull outs [91]. Wear-tested W-3N specimen (Figure 14c) indicated microploughs and microscratches in the Cr-rich region (along the wear direction) [92].

4 Conclusions

Hence, in this investigation, dissimilar joints between AISI 310 and AISI 2205 steels were successfully fabricated using the gas tungsten arc welding process. CO₂ gas and N gas were substituted by 3% in Ar shielding gas during

welding. The corresponding changes in mechanical, machining, and wear characteristics were studied and the following conclusions were drawn:

- i) Reduction in weld bead width (6–7%) was observed on substituting CO₂- and N-substituted shielding gas.
- ii) Tensile tests revealed that UTS, YS, weld region microhardness, and reduction in the percentage of elongation were observed on using 3% CO₂- and N-substituted Ar shielding gas.
- iii) X-RD studies in the weld region indicated the presence of Cr_2C_3 , Fe_2O_3 , $FeCr_2O_4$, σ -Fe, γ -Fe, δ -Fe, Ni. Cr, and Cr_3C_7 compounds.
- iv) Microstructural studies in the welded region showed that δ Fe as elongated lines, γ Fe as cup-shaped structure, and σ phase intermetallics with the high Cr content were observed due to the ferrite-austenite restructuring.
- v) In machining studies, fluctuations in cutting forces were lesser upon increasing the drilling feed rate. For all drilling parameters, weld joints fabricated using N and CO₂ exhibited lower cutting forces after stabilization.
- vi) On evaluating the specific cutting forces in feed direction and cutting direction using local and global analysis approaches, weld joints using CO₂-substituted gas exhibited lower cutting force than the joints fabricated using the N-substituted gas.
- vii) In wear tests, joints using CO₂-substituted gas exhibited better wear characteristics than joints fabricated using N-substituted gas.

Acknowledgements: The authors would like to thank M/s. Vikram Engineering Industry, Tiruchirappalli, for their assistance in conducting welding and drilling experiments. The authors thank National College Instrumentation Facility, National College, Tiruchirappalli, Tamil Nadu, India, for their assistance in microstructural and metallurgical characterizations.

Funding information: No external funding was received for this research.

Author contributions: In this article, Mr. Mahadevan Govindasamy contributed to conceptualization, visualization, writing original draft, and review. Mr. Lloyd Jenner Mangalakaran Joseph Manuel contributed to data curation, investigation, and editing and Mr. Senthilkumar Thamilkolunthu contributed to supervision and validation.

Conflict of interest: Authors state that there is no conflict of interest.

Data availability statement: The authors confirm that the data supporting the findings of this study are available within the article.

References

- [1] Saxena, S. C. Fluidized-bed incineration of solid pellets: Combustion and co-combustion. *Energy Conversion and Management*, Vol. 39, No. 1–2, 1998, pp. 127–141.
- [2] Hirsch, J. Recent development in aluminium for automotive applications. *Transactions of Nonferrous Metals Society of China*, Vol. 24, No. 7, 2014, pp. 1995–2002.
- [3] Sokkalingam, R., V. Muthupandi, K. Sivaprasad, and K. G. Prashanth. Dissimilar welding of AlO. 1CoCrFeNi high-entropy alloy and AISI304 stainless steel. *Journal of Materials Research*, Vol. 34, No. 15, 2019, pp. 2683–2694.
- [4] Dolby, R. E. Advances in welding metallurgy of steel. Metals Technology, Vol. 10, No. 1, 1983, pp. 349-362.
- Moinuddin, S. Q. and A. Sharma. Arc stability and its impact on weld properties and microstructure in anti-phase synchronised synergic-pulsed twin-wire gas metal arc welding. *Materials & Design*, Vol. 67, 2015, pp. 293–302.
- [6] Maurya, A. K., C. Pandey, and R. Chhibber. Dissimilar welding of duplex stainless steel with Ni alloys: A review. *International Journal of Pressure Vessels and Piping*, Vol. 192, 2021, id. 104439.
- [7] Selembo, P. A., M. D. Merrill, and B. E. Logan. The use of stainless steel and nickel alloys as low-cost cathodes in microbial electrolysis cells. *Journal of Power Sources*, Vol. 190, No. 2, 2009, pp. 271–278.
- [8] Newbery, A. P., P. S. Grant, and R. A. Neiser. The velocity and temperature of steel droplets during electric arc spraying. *Surface and Coatings Technology*, Vol. 195, No. 1, 2005, pp. 91–101.
- [9] Saeid, T., A. A. Zadeh, H. Assadi, and F. M. Ghaini. Effect of friction stir welding speed on the microstructure and mechanical properties of a duplex stainless steel. *Materials Science and Engineering: A*, Vol. 496, No. 1–2, 2008, pp. 262–268.
- [10] Aslanlar, S., A. Ogur, U. Ozsarac, E. İlhan, and Z. Demir. Effect of welding current on mechanical properties of galvanized chromided steel sheets in electrical resistance spot welding. *Materials & Design*, Vol. 28, No. 1, 2007, pp. 2–7.
- [11] Haron, C. C., B. M. Deros, A. Ginting, and M. Fauziah. Investigation on the influence of machining parameters when machining tool steel using EDM. *Journal of Materials Processing Technology*, Vol. 116, No. 1, 2001, pp. 84–87.
- [12] Curtin, J. A., E. Quint, V. Tsipouri, R. M. Arkell, B. Cattanach, A. J. Copp, et al. Mutation of Celsr1 disrupts planar polarity of inner ear hair cells and causes severe neural tube defects in the mouse. *Current Biology*, Vol. 13, No. 13, 2003, pp. 1129–1133.
- [13] Cui, J., W. Zhu, Z. Chen, and L. Chen. Effect of simulated cooling time on microstructure and toughness of CGHAZ in novel high-strength low-carbon construction steel. *Science* and *Technology of Welding and Joining*, Vol. 25, No. 2, 2020, pp. 169–177.

- [14] Yan, J., M. Gao, and X. Zeng. Study on microstructure and mechanical properties of 304 stainless steel joints by TIG, laser and laser-TIG hybrid welding. Optics and Lasers in Engineering, Vol. 48, No. 4, 2010, pp. 512-517.
- [15] Gvozdev, A. E., N. N. Sergeyev, I. V. Minayev, A. G. Kolmakov, I. V. Tikhonova, A. N. Sergeyev, et al. Temperature distribution and structure in the heat-affected zone for steel sheets after laser cutting. Inorganic Materials: Applied Research, Vol. 8, No. 1, 2017, pp. 148-152.
- [16] Wang, W., Y. Lu, X. Ding. and T. Shoji. Microstructures and microhardness at fusion boundary of 316 stainless steel/ Inconel 182 dissimilar welding. Materials Characterization, Vol. 107, 2015, pp. 255-261.
- [17] Nielsen, K. L. and V. Tvergaard. Ductile shear failure or plug failure of spot welds modelled by modified Gurson model. Engineering Fracture Mechanics, Vol. 77, No. 7, 2010, pp. 1031-1047.
- [18] Palani, P. K. and N. Murugan. Optimization of weld bead geometry for stainless steel claddings deposited by FCAW. Journal of Materials Processing Technology, Vol. 190, No. 1-3, 2007, pp. 291-299.
- [19] Xie, G., Z. Luo, G. Wang, L. Li, and G. Wang. Interface characteristic and properties of stainless steel/HSLA steel clad plate by vacuum rolling cladding. Materials Transactions, Vol. 1, 2011, id. 1107111433.
- [20] Cross, C. E. On the origin of weld solidification cracking. Hot cracking phenomena in welds, Springer, Berlin, Heidelberg, 2005, pp. 3-18.
- [21] Liu, W., H. Pan, L. Li, H. Lv, Z. Wu, F. Cao, et al. Corrosion behavior of the high strength low alloy steel joined by vertical electro-gas welding and submerged arc welding methods. Journal of Manufacturing Processes, Vol. 25, 2017, pp. 418-425.
- [22] Shi, C. Steel slag—its production, processing, characteristics, and cementitious properties. Journal of Materials in Civil Engineering, Vol. 16, No. 3, 2004, pp. 230-236.
- [23] Chaudhari, A. N., K. Dixit, G. S. Bhatia, B. Singh, P. Singhal, and K. K. Saxena. Welding behaviour of duplex stainless Steel AISI 2205: A Review. Materials Today: Proceedings, Vol. 18, 2019, pp. 2731-2737.
- [24] Soroushian, P. and K. B. Choi. Steel mechanical properties at different strain rates. Journal of Structural Engineering, Vol. 113, No. 4, 1987, pp. 663-672.
- [25] Misra, R. D. K., G. C. Weatherly, J. E. Hartmann, and A. J. Boucek. Ultrahigh strength hot rolled microalloyed steels: Microstructural aspects of development. Materials Science and Technology, Vol. 17, No. 9, 2001, pp. 1119-1129.
- [26] Arafin, M. A. and J. A. Szpunar. A new understanding of intergranular stress corrosion cracking resistance of pipeline steel through grain boundary character and crystallographic texture studies. Corrosion Science, Vol. 51, No. 1, 2009, pp. 119-128.
- [27] Huang, H. Y., S. W. Shyu, K. H. Tseng, and C. P. Chou. Evaluation of TIG flux welding on the characteristics of stainless steel. Science and Technology of Welding and Joining, Vol. 10, No. 5, 2005, pp. 566-573.
- [28] Jarvis, B. L. Keyhole gas tungsten arc welding: A new process variant, Doctoral thesis, Faculty of Engineering, University of Wollongong, Northfields Ave, Wollongong NSW 2522, Australia, 2001. https://ro.uow.edu.au/theses/1833.

- [29] Arivazhagan, B. and M. Kamaraj. A study on factors influencing toughness of basic flux-cored weld of modified 9Cr-1Mo steel. Journal of Materials Engineering and Performance, Vol. 20, No. 7, 2011, pp. 1188-1195.
- Kshirsagar, R., S. Jones, J. Lawrence, and J. Kanfoud. Effect of the addition of nitrogen through shielding gas on tig welds made homogenously and heterogeneously on 300 series austenitic stainless steels. Journal of Manufacturing and Materials Processing, Vol. 5, No. 3, 2021, id. 72.
- [31] Zhang, Z., H. Jing, L. Xu, Y. Han, L. Zhao, and C. Zhou. Effects of nitrogen in shielding gas on microstructure evolution and localized corrosion behavior of duplex stainless steel welding joint. Applied Surface Science, Vol. 404, 2017, pp. 110-128.
- [32] Murphy, A. B., M. Tanaka, S. Tashiro, T. Sato, and J. J. Lowke. A computational investigation of the effectiveness of different shielding gas mixtures for arc welding. Journal of Physics D: Applied Physics, Vol. 42, No. 11, 2009, id. 115205.
- [33] Kah, P. and J. Martikainen. Influence of shielding gases in the welding of metals. The International Journal of Advanced Manufacturing Technology, Vol. 64, No. 9, 2013, pp. 1411-1421.
- Zhang, S., J. Sun, M. Zhu, L. Zhang, P. Nie, and Z. Li. Effects of [34] shielding gases on process stability of 10CrNi3MoV steel in hybrid laser-arc welding. Journal of Materials Processing Technology, Vol. 270, 2019, pp. 37-46.
- Beiranvand, Z. M., F. M. Ghaini, H. N. Moosavy, M. Sheikhi, [35] M. J. Torkamany, and M. Moradi. The relation between magnesium evaporation and laser absorption and weld penetration in pulsed laser welding of aluminum alloys: Experimental and numerical investigations. Optics & Laser Technology, Vol. 128, 2020, id. 106170.
- [36] Bermejo, V., L. Karlsson, L. E. Svensson, K. Hurtig, H. Rasmuson, M. Frodigh, et al. Effect of shielding gas on welding performance and properties of duplex and superduplex stainless steel welds. Welding in the World, Vol. 59, No. 2, 2015, pp. 239-249.
- [37] Silveira, G., J. F. Costa, M. C. Mendes, L. F. G. de Souza, and J. C. Jorge. Microstructure and impact toughness of high strength steel weld metals deposited by MCAW-RE process using different shielding gases. The International Journal of Advanced Manufacturing Technology, Vol. 115, No. 9, 2021, pp. 3105-3120.
- [38] Sadeghi, S., M. A. Najafabadi, Y. Javadi, and M. Mohammadisefat. Using ultrasonic waves and finite element method to evaluate through-thickness residual stresses distribution in the friction stir welding of aluminum plates. Materials & Design, Vol. 52, 2013, pp. 870-880.
- [39] Mourad, A. I., A. Khourshid, and T. Sharef. Gas tungsten arc and laser beam welding processes effects on duplex stainless steel 2205 properties. Materials Science and Engineering: A, Vol. 549, 2012, pp. 105-113.
- [40] LW, T. and C. Chen. Laser beam welding of 2205 duplex stainless steel with metal powder additions. ISIJ International, Vol. 44, No. 10, 2004, pp. 1720-1726.
- [41] Cruz-Hernández, V. L., R. García-Hernández, V. H. López-Morelos, M. A. García-Rentería, and J. González-Sánchez. Intergranular corrosion of AISI 347 stainless steel welds obtained under electromagnetic interaction of low intensity. Materials Letters, Vol. 312, 2022, id. 131679.

- [42] Vasudevan, M. A comparative study on the effect of GTAW processes on the microstructure and mechanical properties of P91 steel weld joints. *Journal of Manufacturing Processes*, Vol. 16, No. 2, 2014, pp. 305–311.
- [43] Gill, J. S. and T. K. Reddy. Effect of weld pool vibration on fatigue strength and tensile strength of stainless-steel butt-welded joints by GTAW process. *Proceedings of the World Congress on Engineering*, London, International Association of Engineers, Vol. 2, 2018, pp. 4–6.
- [44] Paul, C. P., A. Jain, P. Ganesh, J. Negi, and A. K. Nath. Laser rapid manufacturing of Colmonoy-6 components. *Optics and Lasers in Engineering*, Vol. 44, No. 10, 2006, pp. 1096–1109.
- [45] Barrick, E. J. and J. N. DuPont. Microstructural characterization and toughness evaluation of 10 wt% Ni steel weld metal gas tungsten arc and gas metal arc weld fusion zones. *Materials Science and Engineering: A*, Vol. 796, 2020, id. 140043.
- [46] Hertzman, S., R. J. Pettersson, R. Blom, E. Kivineva, and J. Eriksson. Influence of shielding gas composition and welding parameters on the N-content and corrosion properties of welds in N-alloyed stainless steel grades. *ISIJ international*, Vol. 36, No. 7, 1996, pp. 968–976.
- [47] Oleksak, R. P., C. S. Carney, L. Teeter, and O. N. Dogan. Oxidation behavior of welded Fe-based and Ni-based alloys in supercritical CO2. Oxidation of Metals, 2021, Vol. 97, pp. 1–17.
- [48] Zhang, R. H., J. L. Pan, and S. Katayama. The mechanism of penetration increase in A-TIG welding. *Frontiers of Materials Science*, Vol. 5, No. 2, 2011, pp. 109–118.
- [49] Costanza, G., A. Sili, and M. E. Tata. Weldability of austenitic stainless steel by metal arc welding with different shielding gas. *Procedia Structural Integrity*, Vol. 2, 2016, pp. 3508–3514.
- [50] Schmidt, L., S. Hickethier, K. Schricker, and J. P. Bergmann. February. Low-spatter high speed welding by use of local shielding gas flows. *High-Power Laser Materials Processing: Applications*, Diagnostics, and SystemsVIII, 10911, SPIE, 2019, pp. 185–197.
- [51] Yang, K. V., P. Rometsch, T. Jarvis, J. Rao, S. Cao, C. Davies, et al. Porosity formation mechanisms and fatigue response in Al-Si-Mg alloys made by selective laser melting. *Materials Science and Engineering: A*, Vol. 712, 2018, pp. 166–174.
- [52] Otegui, J. L., H. W. Kerr, D. J. Burns, and U. H. Mohaupt. Fatigue crack initiation from defects at weld toes in steel. *International Journal of Pressure Vessels and Piping*, Vol. 38, No. 5, 1989, pp. 385–417.
- [53] Sridhar, R., K. D. Ramkumar, and N. Arivazhagan. Characterization of microstructure, strength, and toughness of dissimilar weldments of Inconel 625 and duplex stainless steel SAF 2205. Acta Metallurgica Sinica (English Letters), Vol. 27, No. 6, 2014, pp. 1018–1030.
- [54] Moteshakker, A., I. Danaee, S. Moeinifar, and A. Ashrafi. Hardness and tensile properties of dissimilar welds joints between SAF 2205 and AISI 316L. Science and Technology of Welding and Joining, Vol. 21, No. 1, 2016, pp. 1–10.
- [55] Ridha Mohammed, G., M. Ishak, S. N. A. S. Ahmad, and H. A. Abdulhadi. Fiber laser welding of dissimilar 2205/304 stainless steel plates. *Metals*, Vol. 7, No. 12, 2017, id. 546.
- [56] Zhang, J., Q. Shen, G. Luo, M. Li, and L. Zhang. Microstructure and bonding strength of diffusion welding of Mo/Cu joints with Ni interlayer. *Materials & Design*, Vol. 39, 2012, pp. 81–86.

- [57] Lin, Y. C. and P. Y. Chen. Effect of nitrogen content and retained ferrite on the residual stress in austenitic stainless steel weldments. *Materials Science and Engineering: A*, Vol. 307, No. 1–2, 2001, pp. 165–171.
- [58] Ballaran, T. B., R. G. Trønnes, and D. J. Frost. Equations of state of CalrO3 perovskite and post-perovskite phases. *American Mineralogist*, Vol. 92, No. 10, 2007, pp. 1760–1763.
- [59] Badji, R., M. Bouabdallah, B. Bacroix, C. Kahloun, K. Bettahar, and N. Kherrouba. Effect of solution treatment temperature on the precipitation kinetic of σ-phase in 2205 duplex stainless steel welds. *Materials Science and Engineering: A*, Vol. 496, No. 1–2, 2008, pp. 447–454.
- [60] Yuri, T., T. Ogata, M. Saito, and Y. Hirayama. Effect of welding structure and δ -ferrite on fatigue properties for TIG welded austenitic stainless steels at cryogenic temperatures. *Cryogenics*, Vol. 40, No. 4–5, 2000, pp. 251–259.
- [61] Eghlimi, A., M. Shamanian, M. Eskandarian, A. Zabolian, and J. A. Szpunar. Characterization of microstructure and texture across dissimilar super duplex/austenitic stainless steel weldment joint by austenitic filler metal. *Materials Characterization*, Vol. 106, 2015, pp. 208–217.
- [62] Robertson, J. The mechanism of high temperature aqueous corrosion of stainless steels. *Corrosion Science*, Vol. 32, No. 4, 1991, pp. 443–465.
- [63] Lagoeiro, L. E. Transformation of magnetite to hematite and its influence on the dissolution of iron oxide minerals. *Journal of Metamorphic Geology*, Vol. 16, No. 3, 1998, pp. 415–423.
- [64] Atsushi, K., A. Gramsch Stephen, Y. Takamitsu, I. Daijo, A. Muhtar, O. Mysen Bjorn, et al. The influence of the Jahn Teller effect at Fe²⁺ on the structure of chromite at high pressure. *Phys Chem Minerals*, Vol. 39, No. 2012, 2012, pp. 131–141.
- [65] Ling, L., P. Guo, C. Shang, and Y. Lu. Effects of oxides produced during welding on oxidation behavior of the 304L welded joint in simulated primary circuit solution of PWR. *Corrosion Science*, Vol. 167, 2020, id. 108515.
- [66] Ayyappan, S., G. Panneerselvam, M. P. Antony, and J. Philip. High temperature stability of surfactant capped CoFe2O4 nanoparticles. *Materials Chemistry and Physics*, Vol. 130, No. 3, 2011, pp. 1300–1306.
- [67] Chuaiphan, W. and L. Srijaroenpramong. Effect of welding speed on microstructures, mechanical properties and corrosion behavior of GTA-welded AISI 201 stainless steel sheets. *Journal of Materials Processing Technology*, Vol. 214, No. 2, 2014, pp. 402–408.
- [68] Xie, M. X., L. J. Zhang, G. F. Zhang, J. X. Zhang, Z. Y. Bi, and P. C. Li. Microstructure and mechanical properties of CP-Ti/X65 bimetallic sheets fabricated by explosive welding and hot rolling. *Materials & Design*, Vol. 87, 2015, pp. 181–197.
- [69] Wang, H., Y. Wang, X. Li, W. Wang, and X. Yang. Influence of assembly gap size on the structure and properties of SUS301L stainless steel laser welded lap joint. *Materials*, Vol. 14, No. 4, 2021, id. 996.
- [70] Ochoa, M., M. A. Rodriguez, and S. B. Farina. Corrosion of high purity copper in solutions containing NaCl, Na₂SO₄ and NaHCO₃ at different temperatures. *Procedia Materials Science*, Vol. 9, 2015, pp. 460–468.
- [71] Zhang, X., Z. Zhu, X. Ma, C. Wang, G. Mi, and S. Zheng. Solidification features and tensile performance altered by

- increased welding speed during laser welding GH909 superalloy. *Materials Characterization*, Vol. 181, 2021, id. 111488.
- [72] Li, J., Y. Liu, Y. Tao, Q. Zhang, Z. Zhen, C. Cai, et al. Energy reconstruction and metallurgical characteristics in 316L NG-LWFW with assisted wire wobbling by numerical and experimental analysis. *Optics & Laser Technology*, Vol. 142, 2021, id. 107242.
- [73] Liu, F. C., T. W. Nelson, S. L. McCracken, and P. Minson. Nanoscale chromium carbides induced abnormal hardness in dissimilar metal welds. *Science and Technology of Welding* and Joining, Vol. 26, No. 4, 2021, pp. 324–331.
- [74] Ozbaysal, K. and O. T. Inal. Thermodynamics and structure of solidification in the fusion zone of CO₂ laser welds of 15-5 PH stainless steel. *Materials Science and Engineering: A*, Vol. 130, No. 2, 1990, pp. 205–217.
- [75] Nage, D. D., V. S. Raja, and R. Raman. Effect of nitrogen addition on the microstructure and mechanical behavior of 317L and 904L austenitic stainless steel welds. *Journal of Materials Science*, Vol. 41, No. 7, 2006, pp. 2097–2112.
- [76] Zhang, Z., H. Jing, L. Xu, Y. Han, L. Zhao, and J. Zhang. Influence of microstructure and elemental partitioning on pitting corrosion resistance of duplex stainless steel welding joints. Applied Surface Science, Vol. 394, 2017, pp. 297–314.
- [77] Schulze, V., C. Becke, K. Weidenmann, and S. Dietrich. Machining strategies for hole making in composites with minimal workpiece damage by directing the process forces inwards. *Journal of Materials Processing Technology*, Vol. 211, No. 3, 2011, pp. 329-338.
- [78] Leshock, C. E., J. N. Kim, and Y. C. Shin. Plasma enhanced machining of Inconel 718: Modeling of workpiece temperature with plasma heating and experimental results. *International Journal of Machine Tools and Manufacture*, Vol. 41, No. 6, 2001, pp. 877–897.
- [79] Namazi, H., A. A. Farid, and T. S. Chang. Fractal-based analysis of the variations of cutting forces along different axes in end milling operation. *Fractals*, Vol. 26, No. 6, 2018, id. 1850089.
- [80] Hastings, W. F., P. Mathew, P. L. B. Oxley, and H. Ford. A machining theory for predicting chip geometry, cutting forces etc. from work material properties and cutting conditions. *Proceedings of the Royal Society of London A Mathematical and Physical Sciences*, Vol. 371, No. 1747, 1980, pp. 569–587.

- [81] Qiu, X., P. Li, Q. Niu, A. Chen, P. Ouyang, C. Li, et al. Influence of machining parameters and tool structure on cutting force and hole wall damage in drilling CFRP with stepped drills. *The International Journal of Advanced Manufacturing Technology*, Vol. 97, No. 1, 2018, pp. 857–865.
- [82] Acaroglu, O. Prediction of thrust and torque requirements of TBMs with fuzzy logic models. *Tunnelling and Underground Space Technology*, Vol. 26, No. 2, 2011, pp. 267–275.
- [83] Franke, V. Drilling of long fiber reinforced thermoplastics influence of the cutting edge on the machining results. CIRP Annals, Vol. 60, No. 1, 2011, pp. 65–68.
- [84] Legrand, C., G. Fromentin, G. Poulachon, R. Chatain, and M. Rancic. A geometrical and mechanistic generalized model for complex shape broaching of super alloy. *Procedia CIRP*, Vol. 82, 2019, pp. 461–466.
- [85] Fu, Z., X. Chen, J. Mao, and T. Xiong. An analytical force mode applied to three-dimensional turning based on a predictive machining theory. *International Journal of Mechanical Sciences*, Vol. 136, 2018, pp. 94–105.
- [86] Budak, E. Analytical models for high performance milling. Part I: Cutting forces, structural deformations and tolerance integrity. *International Journal of Machine Tools and Manufacture*, Vol. 46, No. 12–13, 2006, pp. 1478–1488.
- [87] Służalec, A. Thermal effects in friction welding. *International Journal of Mechanical Sciences*, Vol. 32, No. 6, 1990, pp. 467–478.
- [88] Wolff, R. The influence of surface roughness texture on the temperature and scuffing in sliding contact. Wear, Vol. 143, No. 1, 1991, pp. 99–118.
- [89] Obikawa, T. and E. Usui. Computational machining of titanium alloy—finite element modeling and a few results. *Journal of Manufacturing Science & Engineering*, Vol. 118, No. 2, 1996, pp. 208–215.
- [90] Glaeser, W. Friction and wear. *IEEE Transactions on Parts, Hybrids, and Packaging*, Vol. 7, No. 2, 1971, pp. 99–105.
- [91] Bergant, Z., B. Š. Batič, I. Felde, R. Šturm, and M. Sedlaček. Tribological Properties of Solid Solution Strengthened Laser Cladded NiCrBSi/WC-12Co Metal Matrix Composite Coatings. Materials, Vol. 15, No. 1, 2022, id. 342.
- [92] Krell, J., A. Roettger, and W. Theisen. Comprehensive investigation of the microstructure-property relationship of differently manufactured Co-Cr-C alloys at room and elevated temperature. *Wear*, Vol. 444, 2020, id. 203138.